STATE RESEARCH CENTER OF RUSSIA
INSTITUTE FOR HIGH ENERGY PHYSICS
RU-142284, Protvino, Moscow Region, Russia

NuMI–B–XXX
March 30, 2001

Further Studies of Target for the Low Energy NuMI Beam

S.Filippov, P.Galkin, V.Garkusha, V.Gres, V.Gurov,
V.Lapygin, F.Novoskoltsev, A.Ryabov, A.Shalunov,
V.Zarucheisky

Contents

1 Introduction

The advanced conceptual design of the LE target (the target intended to be used in the NuMI low energy neutrino beam) is described in the NuMI-B-543 Note. Besides to that, the NuMI-B-675 Note gives results of calculations of dynamic stresses arising in the LE target due to very short heat load of a target material by the single turn extracted primary beam, as well as results of LE target prototyping, which were fabricated to test the general construction technics and that alignment tolerances can be met.

In response to recommendations outlined in "The NuMI Low Energy Target Design Review Summary" from October 19, 2000, **Sections 2–5** of this Report present results of the additional design studies, which should allow to make the final choice of LE target parameters and then proceed with production of the final drawing package for this target.

Furthermore, **Section 6** describes briefly two possible methods, which may be used for the remote alignment of target with respect to the horn in case of its initial installation and/or for replacement of a failured target.

2 Results of Energy Deposition, Temperature and Stress Calculations

Cross-section of the LE target is shown in Figure 2.1. The target core is a row of 47 graphite segments, each 3.2 mm wide, 20 mm high and 20 mm long. The segments are soldered to two steel cooling pipes with external diameter 4.0 mm and wall thickness 0.2 mm and inserted into 0.4 mm thick 30 mm diameter aluminum casing.

The effect of neutrino flux reduction due to absorption of secondaries in the accepted target geometry is shown in Figure 2.2. The total number of ν_μ CC events in the far detector provided by the LE target is only 4–5% smaller with respect to that provided by the hypothetical 3.2×6.4 mm^2 rod target with the same length and density as in the considered target design.

2.1 Energy Deposition in the Target

Results of energy deposition calculations are shown in Figure 2.3. Calculations were made using the official Fermilab MARS version for the primary proton beam with Gaussian distributions in both transverse directions $\sigma_x \times \sigma_y = 0.7 \times 1.4$ mm^2.

The energy deposition density at the beam axis reaches the maximal value of $\sim$0.095 GeV/cm^3/proton in 4$\div$6 segments and then decreases continuously to $\sim$0.025 GeV/cm^3/proton at the downstream end of the target. Distributions of average power deposited in the target are given for the primary beam with intensity of 4×10^{13} protons per 1.9 s. The power deposited in target segments is equal to 2.06 kW. With addition of 0.125 kW deposited in steel pipes and in cooling water, the total load to the water cooling system is about 2.2 kW. Energy depositions in other main components of the LE target design are given in Table 2.1.

Input window (0.5 mm thick Be)	0.81
Aluminum target canister	2.20
Ceramic adapter (Al_2O_3)	0.47
Stainless steel flange	15.7
Aluminum target casing	118
Output window (0.5 mm thick Be)	2.93

Table 2.1: Energy deposition (W) in some components of the LE target.

2.2 Cooling of Target Segments

Calculated values of a heat transfer coefficient, a pressure drop, a flow rate and a temperature rise of a cooling water as functions of a water flow velocity in the target cooling system are given in Table 2.2. Calculations were made for cooling pipes with internal diameter of 3.6 mm and roughness of 0.02 mm. Taking into account that the input temperature of a cooling water is equal to 37°C, a relatively wide range of water flow velocities from 2 up to 4 m/s is acceptable for cooling of target segments.

Velocity of a cooling water, m/s	2	3	4
Heat transfer coefficient, kW/m^2/K	11	15	19
Pressure drop, atm	0.53	1.1	1.9
Water flow rate, l/min	1.2	1.8	2.4
Water temperature rise, °C	26	17	13

Table 2.2: Main parameters of a cooling system.

2.3 Temperature and Stresses in Target Segments

Calculations of target temperature, as well as stresses induced in a target material by the single turn extracted primary beam with $\tau \simeq 8$ μs were made by the ANSYS under the following boundary conditions:

- the thermo-resistance between a target material and cooling pipes is assumed to be zero. The input temperature of cooling water is equal to 37°C;
- a heat transfer coefficient to the ambient atmosphere is equal to zero, i.e. the target is in vacuum.
- for thermal radiation, target segments have an emissivity of 1.0 and the ambient temperature is 20°C.

No prestress of the material was included in stress calculations. Despite of the some difference in thermal expansion coefficients of the graphite and cooling pipe steel [1], the high plasticity soft solder, used for soldering of target segments to cooling pipes, prevents arising of stresses in graphite during cooling of the soldered assembly from ~300°C to the room temperature.

[1] Thermal expansion coefficients of the ZXF-5Q graphite and steel used for production of cooling pipes are equal to 8.1×10^{-6} and 10.2×10^{-6} 1/K at 20°C , and almost equally increase with a temperature.

Results of calculations of temperature and stresses in a target segment with the highest energy deposition density for the case of cooling water velocity equal to 2 m/s are shown in Figure 2.4–2.6, while Table 2.3 gives target temperature and stresses for two different operation modes of a cooling system. Comparison of these results with those obtained without thermal radiation shows its relatively small influence on the steady-state temperature of a target.

Velocity of a cooling water, m/s	2	4
Temperature before beam spill, °C	95	79
Temperature after beam spill, °C	351	340
Maximal equivalent stress at the center of a segment, MPa	27.9	28.3
Maximal equivalent stress at the rounded corner of a segment, MPa	29.1	29.4

Table 2.3: Temperatures at the beam axis and maximal thermal stresses in a target segment with the highest energy deposition density for two operation modes of a cooling system.

Since the graphite has different compressive and tensile strength limits, which are equal to 210 MPa and 95 MPa respectively for used ZXF–5Q grade with density of 1.81 g/cm^3, the crucial point for a target material integrity is at the rounded corner of segment where graphite is subjected to all-axis stretch. Taking into account that the high cycle fatigue endurance limit of graphite is in the range of 0.5–0.6, the safety factor (the ratio of the fatigue endurance limit to the maximal equivalent stress occurring in target segments) is about 1.8.

2.4 Extended Stress Calculations

Temperature and stress calculations were made using one type of grid consisting of 12488 elements in 1/4 of a target segment (Figure 2.7). To verify given above results, calculation were repeated with the 2 times small-sized grid consisting of 2^3 times larger number of elements. As was found, the "double" grid gives the 1% increase of maximal temperature and 3–4% increase of maximal stresses in a target segment with the highest energy deposition density with respect to those obtained with the baseline grid.

2.5 Potentials of the Safety Factor Increase

The most efficient way to increase the design value of a safety factor is an increase of the primary beam spot size (resulting in decrease of the energy deposition density with subsequent decrease of the adiabatic temperature rise and thermal stresses in the target material). Further stretching of the proton beam in the vertical direction will not change neutrino flux, whereas an increase of the proton beam width and corresponding increase of the segment width will decrease neutrino flux due to extra absorption of secondaries in the target material. This is illustrated by results of temperature and stress calculations given in Table 2.4 for three different variants of the LE target.

To minimize absorption of secondaries in the 4.8 mm wide target, the width of segments was increased only in their central part occupied by the primary proton beam (Figure 2.8). In this case the total number of ν_μ CC events with $E_\nu \leq 6$ GeV is only 1.5% smaller than that for the baseline 3.2 mm wide LE target. The use of target segments with constant in the vertical direction width of 4.8 mm provides more easy machining, but increases the loss of neutrino events up to 3% [2].

Width of a target segment, mm	3.2 (baseline)	3.2	4.8	4.8
Primary beam spot size $\sigma_x \times \sigma_y$, mm^2	0.7×1.4	0.7×1.8	0.7×1.4	1.05×1.8
Energy deposition density, GeV/cm^3	0.095	0.073	0.095	0.055
Temperature before beam spill, °C	94.8	94.6	98.7	101
Temperature rise, °C	256	208	253	162
Temperature after beam spill, °C	351	303	351	263
Maximal equivalent stress at the center of a segment (all-axis compression), MPa	27.9	23.3	27.9	18.2
Maximal equivalent stress at the rounded corner of a segment (all-axis stretch), MPa	29.1	23.8	26.0	18.8
Safety factor	1.8	2.2	2.0	2.8

Table 2.4: Temperatures and maximal thermal stresses in target segments with the highest energy deposition density for different LE targets.

[2] One should note, that for both variants of the 4.8 mm wide target the loss of neutrino events in comparison with the 3.2 mm wide target takes place only for neutrinos with $3 \leq E_\nu \leq 6$ GeV. The lowest energy part of the spectrum remains almost without changes.

2.6 Temperature of Target Casing

The average power deposited in the 0.4 mm thick aluminum casing is about 120 W (Table 2.1). As it follows from longitudinal distribution of an energy deposition (Figure 2.3c), the maximal temperature of casing is expected at its downstream end.

Assuming a vacuum inside the target, cooling of target segments (by means of the water in steel pipes) and cooling of target casing (by means of the air flow) may be considered independently. The maximal temperature of target casing as a function of the air flow velocity is shown in Figure 2.9, while Figure 2.10 shows longitudinal distributions of the target casing temperature at $V = 5$ m/s in comparison with the average temperature at the axis of target segments. Since an accurate prediction of the cooling air temperature and flow character in the given geometry is a very difficult task, calculations were made for longitudinal and transverse directions of the low turbulence air flow with the temperature of 20°C. Larger values of the heat transfer coefficient and, correspondingly, lower temperatures of target casing one should expect in the case of high turbulence air flow.

In the case of helium filled target the precise thermal model should take into account the heat exchange between water cooled graphite segments and air cooled target casing. On the other hand, estimations show that a week natural convection of helium inside the target casing, if any, and much less the thermal conductivity of helium, can not provide a noticeable heat removal from the lateral sides of target segments and, as a result, additional heating of target casing.

2.7 Target Failure Detection by means of Calorimetry on the Cooling Water

Neutrino beam simulations show, that the "disappearance" of one segment in the first part of target will cause the 3–4% decrease of neutrino events with $E_\nu < 6$ GeV in the far detector. To investigate whether this failure could be detected by performing calorimetry on the cooling water, calculations of the energy deposition were repeated for the baseline target with missing 5-th segment (the segment with the highest energy deposition density and, correspondingly, with highest stresses). As was found, the total average power deposited in target segments and in the cooling system de-

creased at ~2.3% from 2.19 kW in the perfect target to 2.14 kW in the failured one.

Since for the cooling system

$$P = C_p \rho Q \Delta T,$$

where P is the total load to the cooling system (W), C_p and ρ are the specific heat (J/kg/K) and the density (kg/m^3) of a cooling water, Q is the water flow rate (m^3/s) and ΔT is the difference (K) between water temperatures at the input and output of a cooling system; variation of the power deposited in the target can be detected by long-term measurements of the flow rate and temperature rise of a cooling water. Taking into account that the difference between water temperatures at the input and output of a cooling system can be measured with a relatively high accuracy ($\leq$0.1°C), the measurement of the water flow rate with the accuracy $\leq$1% is required to detect the "disappearance" of one target segment.

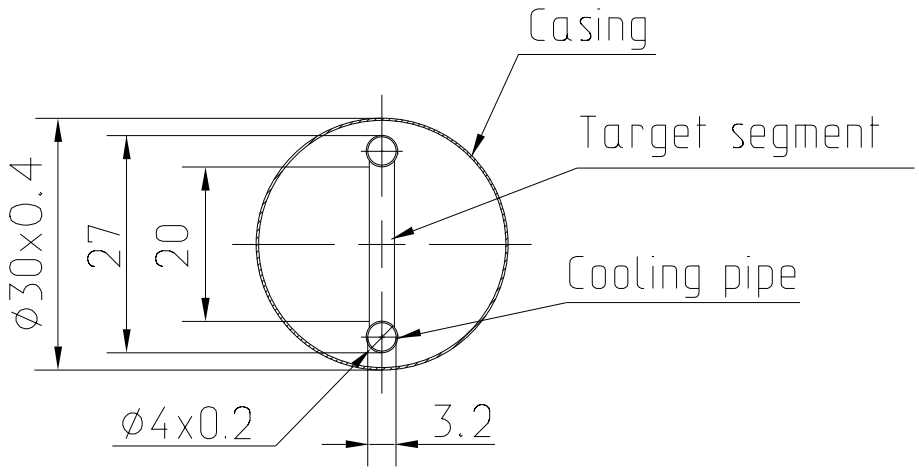

Figure 2.1: Cross-section of the LE target.

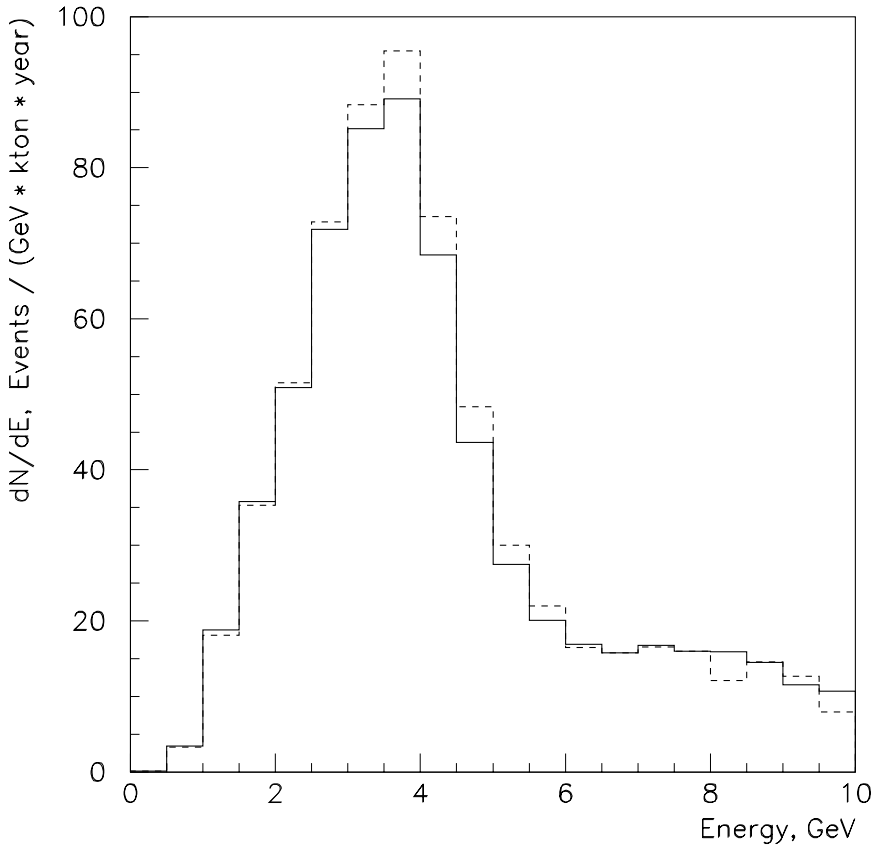

Figure 2.2: Low energy beam spectrum of ν_μ CC events for the water cooled fin target shown in Figure 2.1 (solid line) in comparison with that for the 3.2×6.4 mm^2 bare target (dash line).

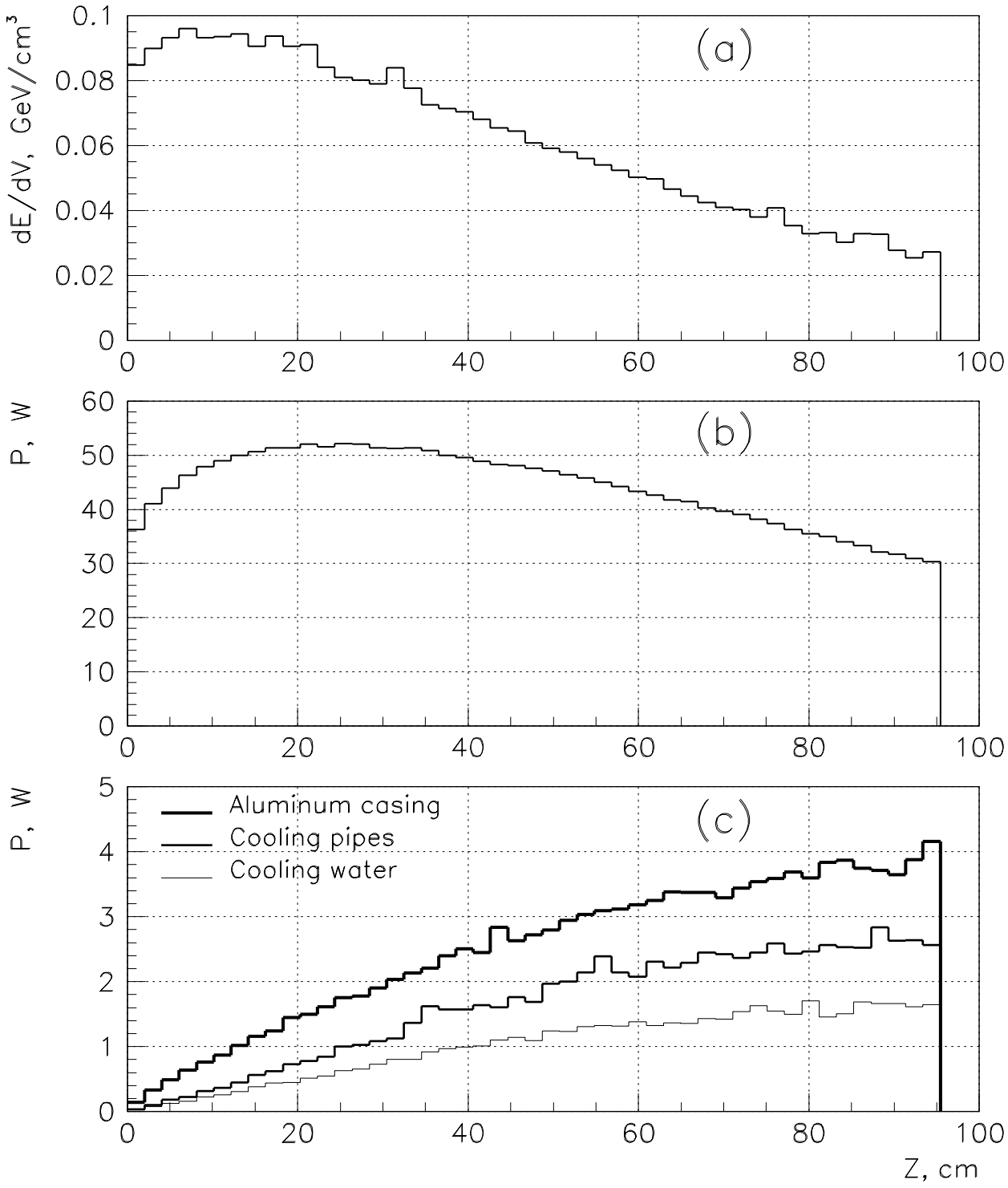

Figure 2.3: The energy deposition density at the beam axis in graphite target segments (a), and the average power deposited in target segments (b) and in main parts of the target design (c).

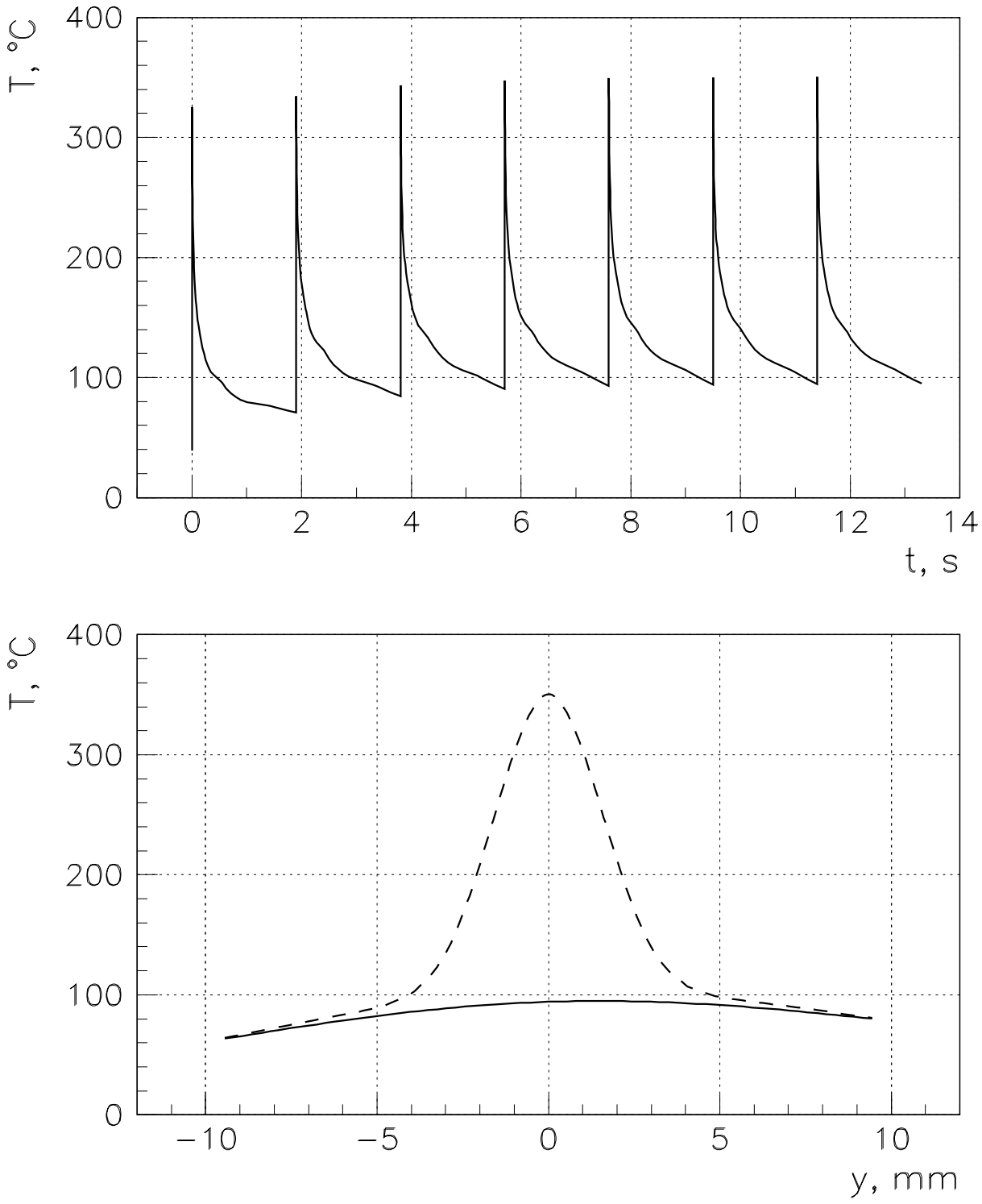

Figure 2.4: Time evolution of temperature at the center (top) and temperature distribution along the vertical axis of a target segment with the highest energy deposition density (bottom).

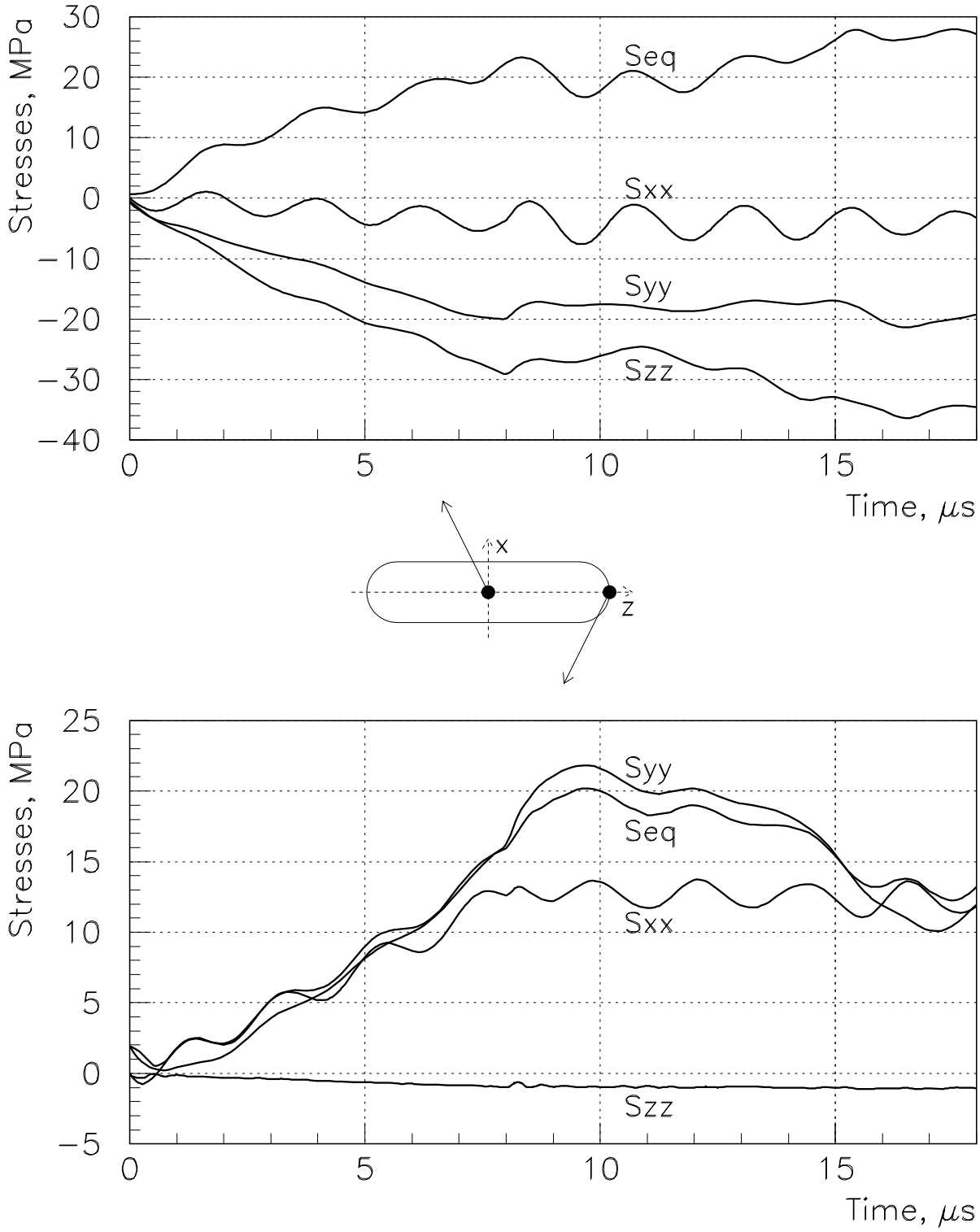

Figure 2.5: Time evolution of stresses at two points of the beam axis plane in a target segment with the highest energy deposition density.

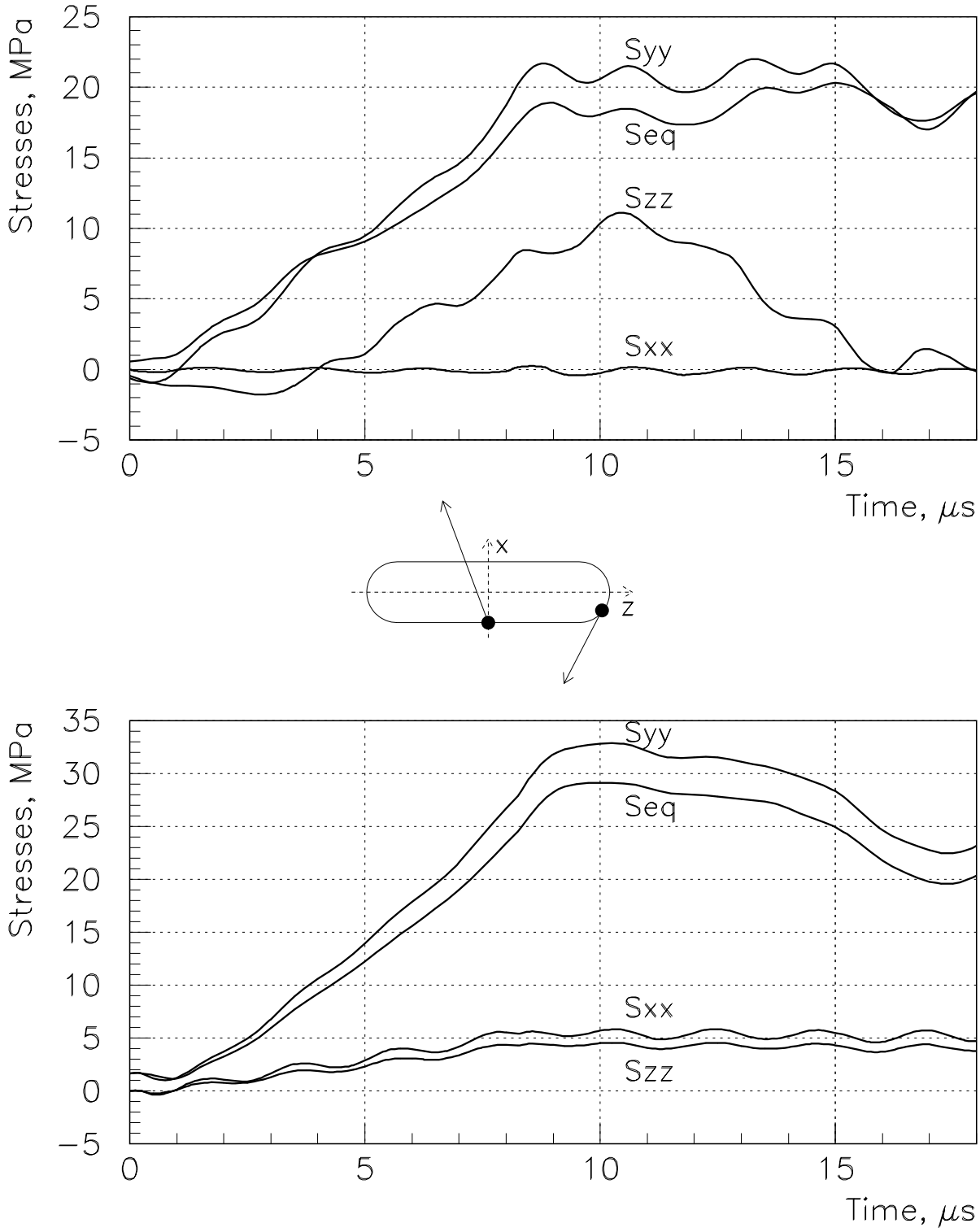

Figure 2.6: Time evolution of stresses at two points of the beam axis plane in a target segment with the highest energy deposition density.

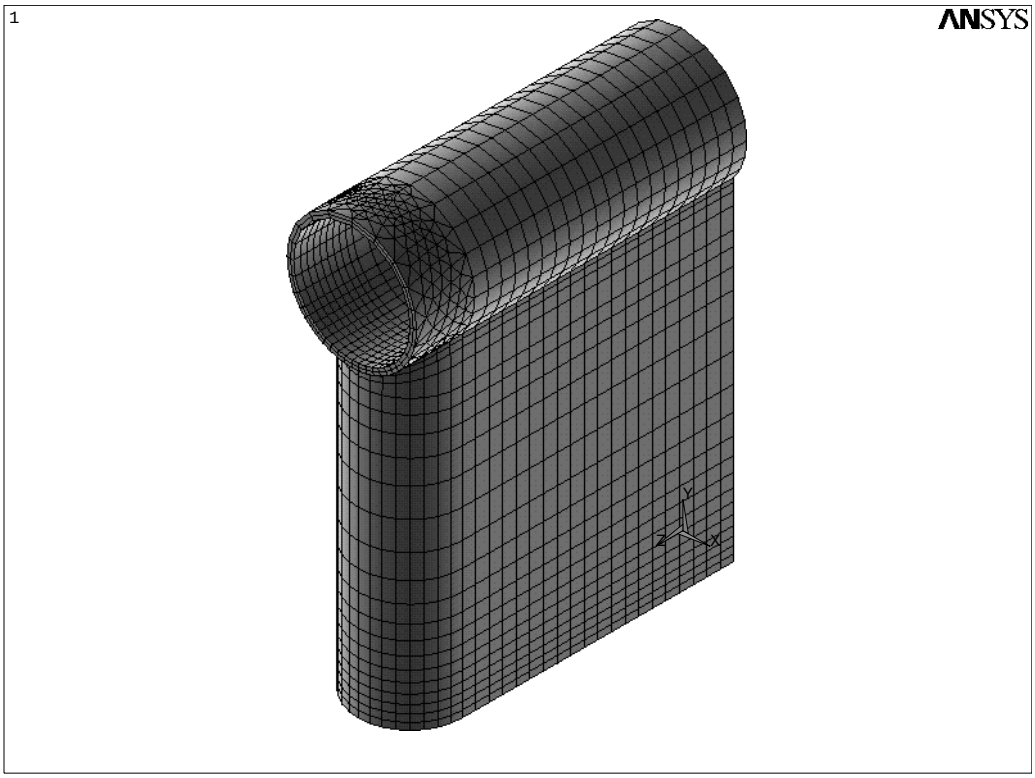

Figure 2.7: The baseline grid used in ANSYS simulations.

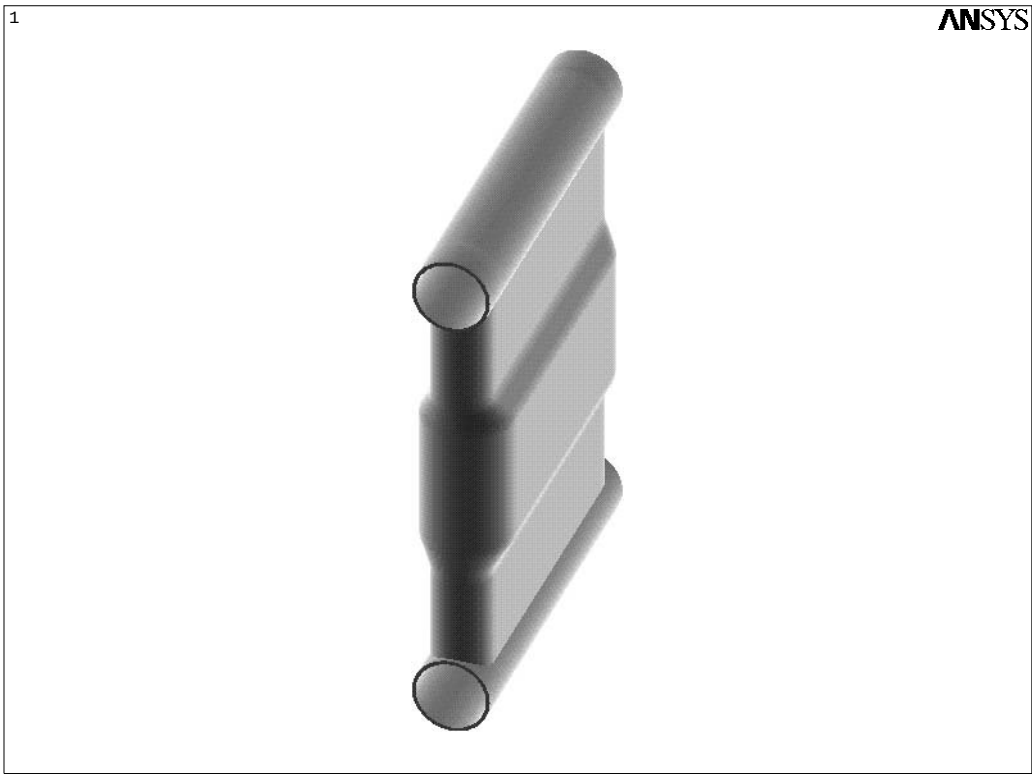

Figure 2.8: The ANSYS model of the 4.8 mm wide target segment.

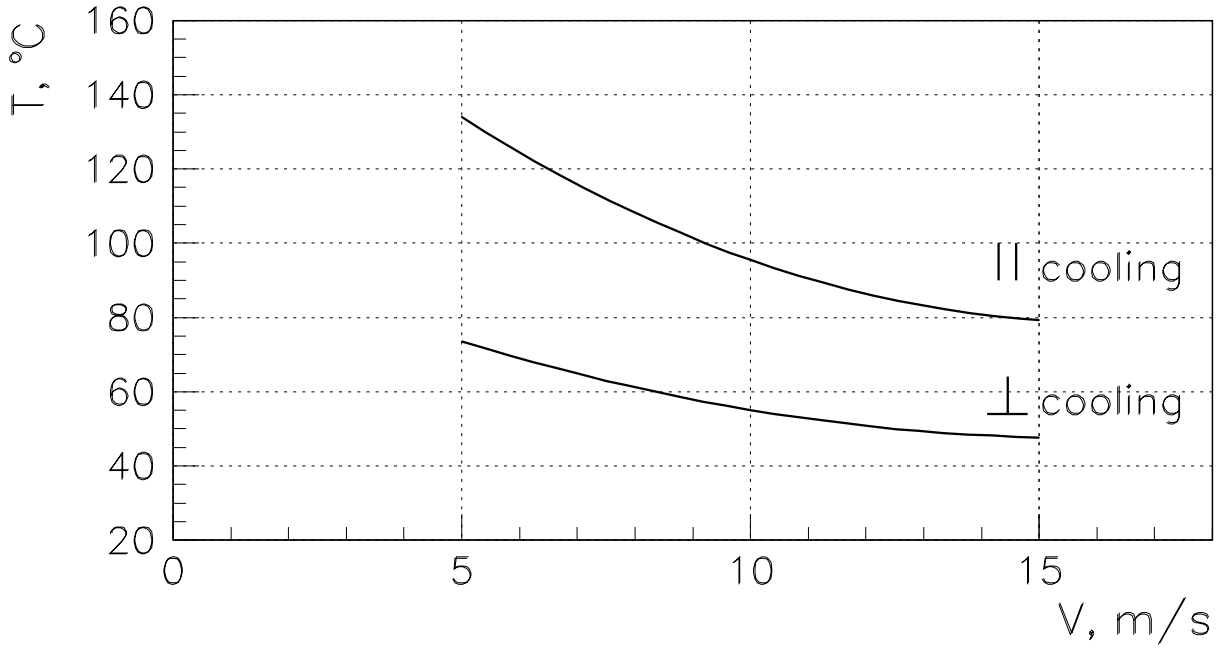

Figure 2.9: Maximal temperatures of target casing (at its downstream end) as functions of the cooling air velocity for a target with vacuum inside.

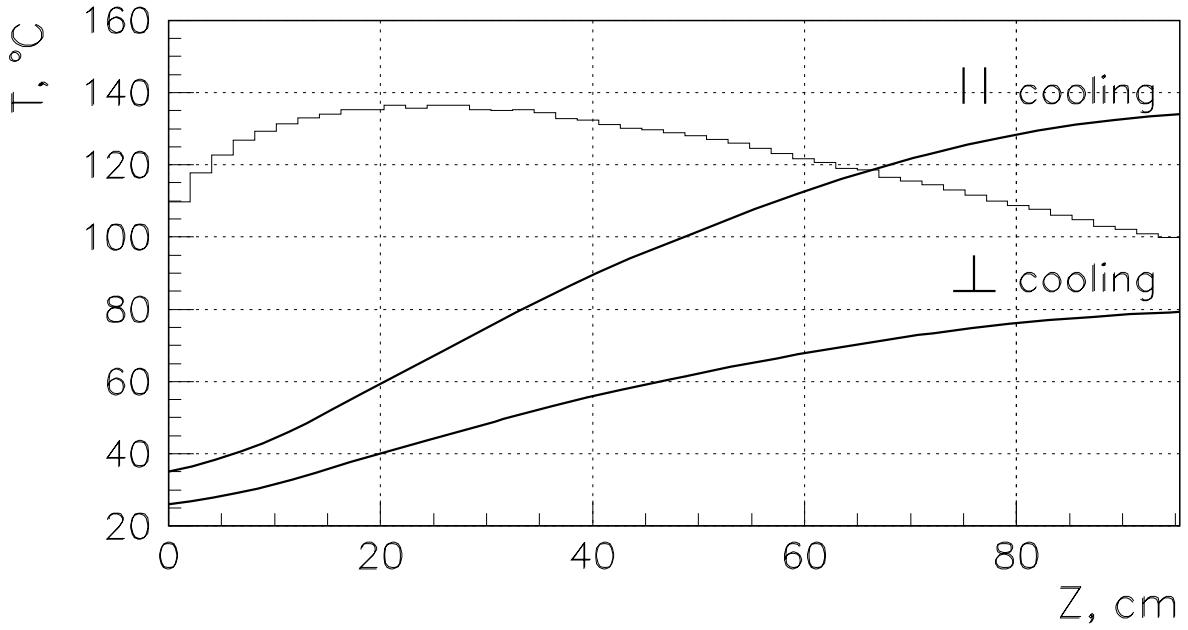

Figure 2.10: Longitudinal distributions of the target casing temperature at $V = 5$ m/s and the average temperature at the axis of target segments (histogram) for a target with vacuum inside.

3 Radiation Damage in Graphite

It is well known that irradiation of graphite with reactor neutrons leads to dimensional changes of considerable magnitude, as well as to changes of its thermo-physical and mechanical properties [1]. Figures 3.1 and 3.2 show variations of dimensions and thermal expansion coefficients with the neutron dose for AXF-8Q1 and AXZ-5Q1 Poco graphite grades. These graphites are unusual in showing volume growth or a high degree of stability at most irradiation temperatures. Fractional changes in thermal resistance of graphite are illustrated by the example of the Pile Grade A (PGA) graphite (Figure 3.3).

The effect of irradiation with fast neutrons on the elastic modulus is to initially increase by substantial factors, depending upon the material, at low doses, followed by subsequent increases and decreases. Changes in elastic modulus of H-451 graphite at various irradiation temperatures are shown in Figure 3.4 [2]. On the other hand, the strength of graphite increases with irradiation to a point where the properties decline due to large structural effects [1]. Up to this point the strength in tension and shear increases according to

$$\sigma \geq \sigma_0 \sqrt{E/E_0},$$

where σ_0 is the unirradiated strength in the same direction and mode, E and E_0 are the irradiated and unirradiated values of elastic modulus.

To use these data for evaluation of the LE target lifetime, it is necessary to calculate the dpa (displacements per atom) damage in graphite target segments irradiated by the 120 GeV proton beam. Given below is an attempt to estimate in order of magnitude the dpa damage rate in the LE target without complicated calculations.

The number of displacements per atom in material is [3]

$$N = \int_{E_{min}}^{E_{max}} f(E)dE \int_{E_d}^{T_{max}} \sigma(E,T)\nu(T)dT, \qquad (1)$$

where $f(E)$ is the flux of irradiated particles, $\sigma(E,T)$ is the cross-section for a particle of energy E to produce an atom recoil with energies in the range from T to $T+dT$, $E_d = 25 \div 60$ eV is the energy required to produce the displaced atom in graphite, T_{max} is the maximal energy which can be

transferred to atoms by the incident particle of energy E, and $\nu(T)$ is the number of atomic displacements due to a knock-on primary displacement of energy T (radiation damage function). The function $\nu(T)$ is:

$$\nu(T) = \begin{cases} 0, & T \leq E_d \ , \\ 1, & E_d \leq T \leq 2E_d, \end{cases}$$

and for higher transferred energies to a good approximation [1]

$$\nu(T) = \frac{T}{2E_d}[1 + Kg(\varepsilon)]^{-1},$$

$$g(\varepsilon) = 3.4008\varepsilon^{1/6} + 0.40244\varepsilon^{3/4} + \varepsilon,$$

where $\varepsilon = T/E_l$, and for carbon atoms $K = 0.12748$ and $E_l = 5687$ eV. $\nu(T)$ has the maximal value of $E_l/(2E_dK)$ and at $E_d = 25$ eV reaches about 10^3 even at $T \sim 1$ MeV (Figure 3.5).

Based on (1) the number of atomic displacements may be estimated as

$$N < \int_{E_{min}}^{E_{max}} f(E)\sigma_t(E)\nu(E)dE, \qquad (2)$$

where σ_t is the total cross-section of carbon nucleus for irradiated particles. We note that for 10^{21} cm^{-2} neutrons with the energy of 2 MeV expression (2) gives the number of atomic displacements in graphite $N \simeq 1.6$ dpa, while for reactor neutrons ($E \leq 10$ MeV, the mean energy is $\sim$2 MeV) 1 dpa in graphite corresponds to approximately 10^{21} n/cm^2 [1].

For the $I_{pp} = 3.7 \times 10^{20}$ protons/year NuMI primary beam with the Gaussian distribution in the target and $\sigma_x = 0.07$ cm, $\sigma_y = 0.14$ cm:

1) The number of atomic displacements produced by the primary proton beam itself in the first target segment was estimated using expression (2) with $f(E) = I_{pp}\,/\,(2\pi\sigma_x\sigma_y) = 6 \times 10^{21}$ cm^{-2}. Taking $\sigma_t = 330$ mb and $\nu = 900$ one has $N \simeq 1.8$ dpa/year.

2) Fluxes of all hadrons should be taken into account for calculation of the dpa damage rate in subsequent target segments. Figure 3.6 shows energy spectra of hadrons calculated by MARS in the central part of target segment with highest energy deposition (the peak in the last energy bin for proton spectrum corresponds to non-interacted primary protons). The number of atomic displacements produced in the graphite by neutrons of all energies and charged hadrons with $E \geq 50$ MeV was estimated using

the expression (2) with $\sigma_t(E)$ from [4] and [1]. The expression (1) with differential Coulomb cross-section was used to estimate the number of atomic displacements produced by charged hadrons with $E \leq 50$ MeV. As a result, the total number of atomic displacements produced in the central part of 11-th target segment is $N \simeq 1.9$ dpa/year with $\sim$90% contribution from charged hadrons with the energy $E > 1 - 2$ GeV.

Obtained results suggest that the 1 year lifetime is quite achievable for the LE target from the point of view of the dpa damage in graphite since:

- the ~ 2 dpa level of radiation damage will not cause a noticeable dimensional changes in graphite;
- an increase in the thermal resistance and subsequent increase of the target temperature will lead even to some decrease of thermal stresses;
- an increase in elastic modulus by a factor of two[3] may be compensated by radiation strengthening of graphite and by a proper choice of the safety factor.

On the other hand, the knowledge of only dpa damage rate in graphite not allows to make a final conclusion about the lifetime of a target irradiated by the high energy proton beam. Besides of atomic displacements, the target lifetime will be determined also by generation of a helium, which will release in the form of small bubbles and cause a macroscopic increase of crystals.

[3]Due to the different type of graphite used in the LE target design, one cannot apply directly the data shown in Figures 3.3 and 3.4.

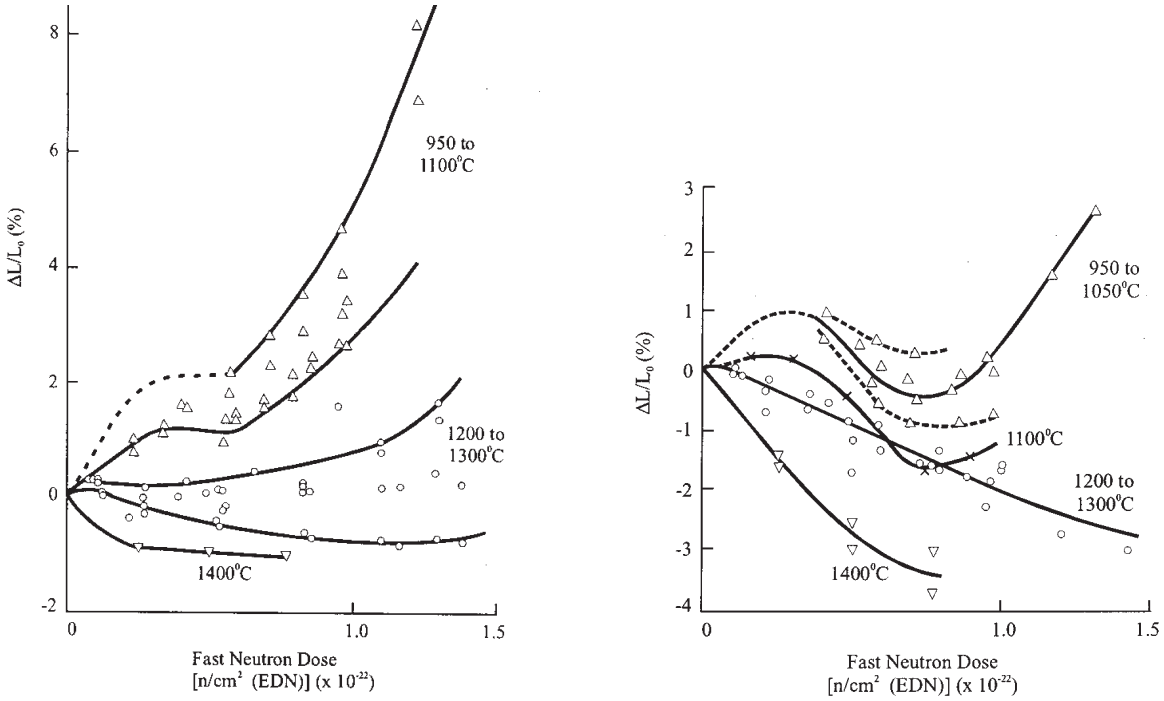

Figure 3.1: Dimensional changes of AXF-8Q1 (left) and AXZ-5Q1 (right) Poco graphite grades.

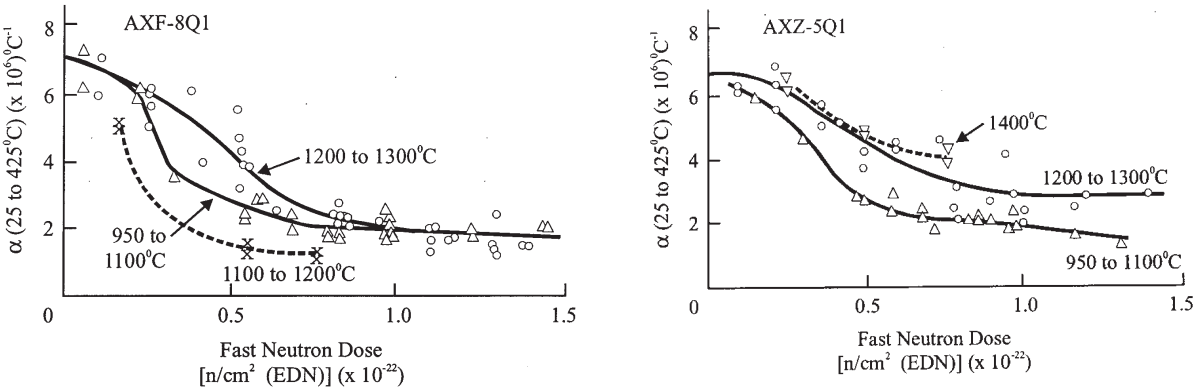

Figure 3.2: Thermal expansion coefficients of AXF-8Q1 (left) and AXZ-5Q1 (right) Poco graphite grades.

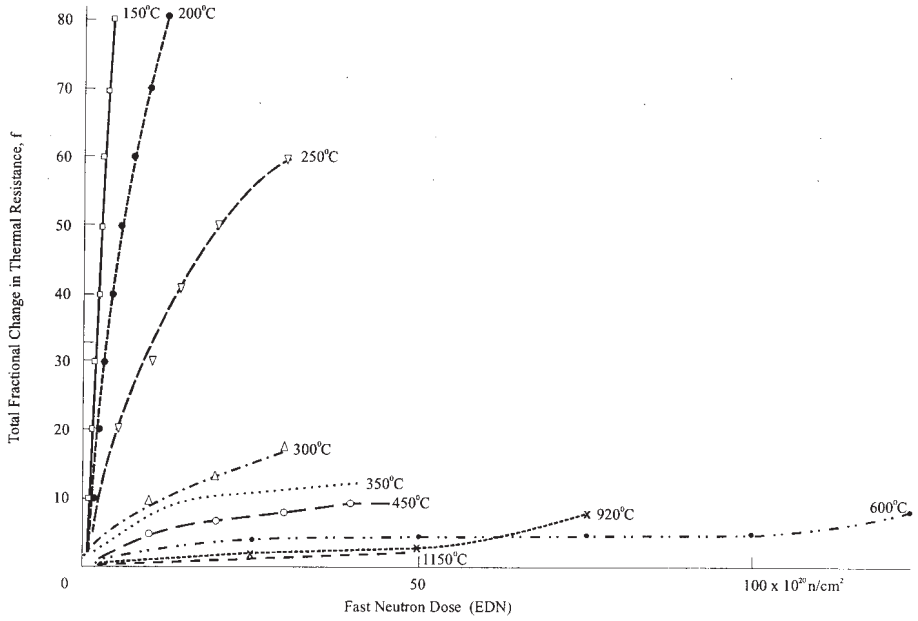

Figure 3.3: Fractional changes in thermal resistance of PGA graphite at various irradiation temperatures.

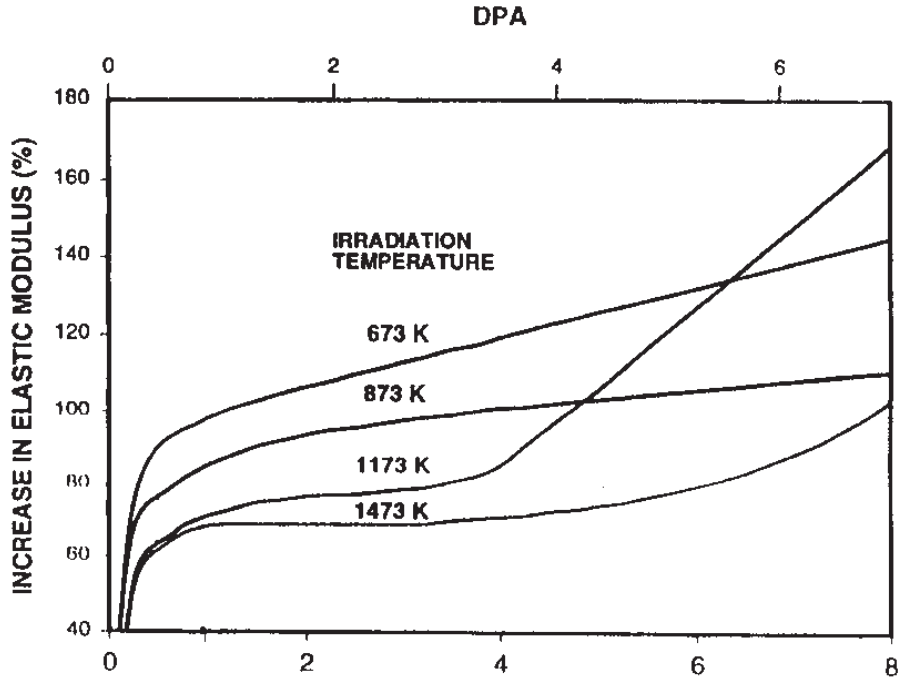

Figure 3.4: Changes in elastic modulus of H-451 graphite as functions of irradiation conditions.

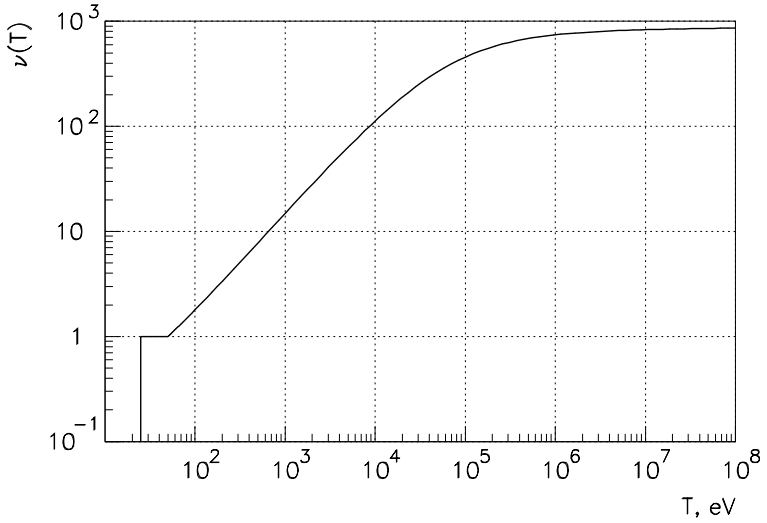

Figure 3.5: The number of atomic displacements $\nu(T)$ due to a primary displacement of energy T.

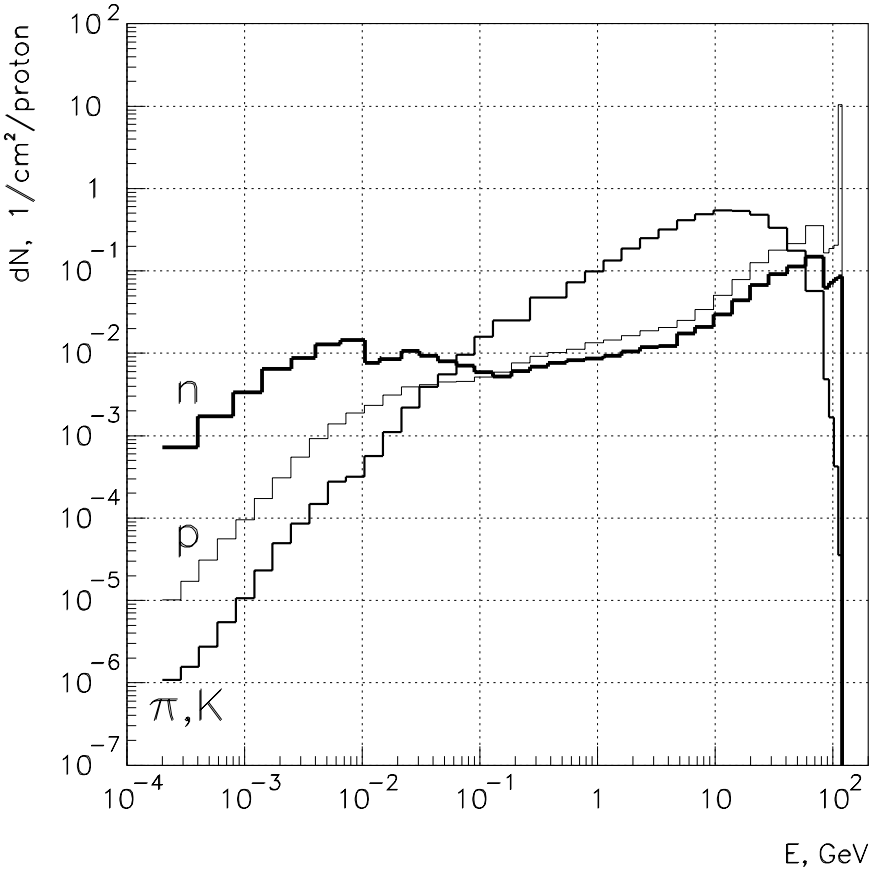

Figure 3.6: Energy spectra of hadrons at the beam axis of 11-th segment.

4 Effects of Highly Ionized Environment near the LE Target

4.1 Equivalent Electric Circuit of the LE Target

An equivalent electric circuit of the LE target during its hitting by a proton beam is shown in Figure 4.1. R_c is the resistance of ceramic adapter to the ground, C_c is the capacitor of target casing to the ground, R_{cf}^{air} is the resistance of ionized air between the flange and ceramic adapter, R_{ct} and C_{ct} are the resistance and the capacitor between graphite segments and target casing, R_w is the resistance of water inside ceramic adapters in water cooling pipes, C_{ch} is the capacitor between the horn and target casing, R_{ch}^{air} is the resistance of air between the horn and target casing. The values of R_{ch}^{air}, R_{ct}, R_{cf}^{air} and R_w depend on the degree of ionization in the area where they are located.

4.2 Ionization in Different Parts of the LE Target

The number of pairs produced by ionizing particles in a unit of volume is [5] $N_{e,i} = (dE/dV)/w_i$, where dE/dV is the density of energy deposition and w_i is the effective average energy to produce one pair (33 eV for an air and 31 eV for a water). The densities of energy deposition per one incident proton calculated with help of the MARS14 code for different parts of the target design and the total number of pairs N_0 for the 4×10^{13} protons/spill primary beam are given in Table 4.1 (see also Figure 4.2).

The ionized volume	dE/dV, keV/cm^3/pot	N_0, cm^{-3}
The air between the horn and target casing	~1.0 (ave.)	1.2×10^{15}
The air near the ceramic adapter of target casing	0.005	6.0×10^{12}
The water inside ceramic adapters of water pipes	0.14	1.8×10^{14}

Table 4.1. Energy deposition densities in different parts of a target.

Because of the relatively small number of pairs (the number of gas molecules in cubic cm of air is 2.7×10^{19}), the air may be considered as a weakly ionized plasma. The conductivity of a weakly ionized plasma is defined mainly by electrons, as they have the mobility which is two order of magnitude higher than the mobility of ions [6].

The instant density of ion pairs in a volume of an air or water depends also on process of recombination of ions. A positive ion can be neutralized recombining in the gas (water) volume with a negative charge carrier, either an electron or negative ion. Electron can be neutralized by ion, or can be attached to a molecule of oxygen or water having electron affinity (electro–negative). Average life time τ_e of electron to be attached is 0.14 μs in a water and 0.19 μs in an air [5].

If N_e and N_+ are the densities of electrons and positive ions respectively, then processes of ions recombination and attachment of electrons can be described by differential equations:

$$\begin{aligned} \frac{dN_e}{dt} &= \frac{N_0}{t_p} - r_e N_e N_+ - \frac{N_e}{\tau_e}, \\ \frac{dN_+}{dt} &= \frac{N_0}{t_p} - r_e N_e N_+ - r_i N_+ (N_+ - N_e), \end{aligned}$$

where $t_p = 8.6$ μs is the duration of extraction, $N_+ - N_e$ is the number of negative ions, r_e and r_i are the coefficients of electron–ion and ion–ion recombinations respectively. Typical value of r_i is about 10^{-6} cm^3/s [7] and $r_e \sim (10^{-8} \div 10^{-7})$ cm^3/s [8].

Time evolution of electron and ion densities, obtained by solving of given above differential equations, are shown in Figure 4.3. Knowledge of an electron velocity in the electric field allows to calculate the equivalent conductivity of an ionized area.

4.3 Conductivity of an Ionized Air

4.3.1 Air Gap between the Horn and Target Casing

Electrons in the air gap between horn and target casing are drifting in the electric field defined by the horn voltage of 47 V [9] and by the distance between horn and casing. At a minimum distance equal to 5 mm, the average electric field is about 100 V/cm. There is a small concentration of the electric field at the corner of casing downstream end. At the radius of corner rounding about 0.4 mm the maximal electric field on the rounding surface is $\sim$1.8 higher than the average field.

Drift velocities of electrons in nitrogen and oxygen as function of the electric field strength are shown in Figure 4.4 [8]. Drifting in the electric field they may get an energy about $E \cdot \Delta S$, where $\Delta S = V_d \tau_e$. Substituting

E, V_d and τ_e for nitrogen one can get that the maximal energy of electrons is about 15 eV, what is smaller than the average effective energy to produce one pair. It means that the density of electrons N_e will be defined by their generation by ionizing particles, attachment by molecules and recombination. In this case the conductivity of ionized air may be calculated as $\sigma = e\mu N_e$, where e is the electron charge, $\mu = \mu_o\mu_n/(\mu_o+\mu_n)$ is the mobility of electrons in air, μ_o and μ_n are the mobilities of electrons in oxygen and nitrogen at the field strength $E \sim 100$ V/cm. Using dependencies of drift velocities in both gases one can get $\mu = 2 \times 10^3$ cm^2/V/s.

At the electron density $N_e = 3 \times 10^{13}$ cm^{-3} (Figure 4.3) the conductivity of air is $\sigma_e = 9.6 \times 10^{-3}$ Ohm^{-1}cm^{-1} and the equivalent specific resistance $\rho_e \simeq 100$ Ohm·cm. Taking into account the large area between horn and target casing and relatively small gap (about one cm) it means that voltage of target casing will be practically equal to the horn voltage. The maximal ionized current in this case will be defined mainly by the resistance R_{cf}^{air} of the air gap between target casing and the flange of target canister.

4.3.2 Air Gap between Target Casing and the Flange of Target Canister

In this area the air gap is equal to 2.5 mm (Figure 4.5) and the average electric field is ~170 V/cm. Thus the mobility of electrons is 1.5×10^3 cm^2/V/s. At the electron density $N_e = 1.3 \times 10^{11}$ cm^{-3} (Figure 4.3), the conductivity of air is $\sigma_e = 3 \times 10^{-5}$ Ohm^{-1}cm^{-1} and the equivalent specific resistance $\rho_e \simeq 3 \times 10^4$ Ohm·cm.

For the 10 mm wide air gap one can get that $R_{cf}^{air} \simeq 1.2$ kOhm. It corresponds to the pulsed current from target casing to the ground about 40 mA. This current may be decreased with help of an additional ceramic ring inserted in this gap as it is shown in Figure 4.5.

4.4 Impact of Radiation to the Water Resistance

No data were found for the electron mobility in a water. In order to estimate it one can use the data for mobility in the water vapor at very low field, i.e. at low ratio of E/N, where E is the electric field strength, N is the number of molecules in cubic centimeter. Extrapolating the data given in [8] one can get for the electron mobility in a water $\mu_e^w = 92.6$ cm^2/V/s.

For given above values of coefficients r_e, r_i the density of electrons is $N_e \simeq 2.9 \times 10^{12}$ cm^{-3} and the equivalent specific resistance $\rho_e^w \simeq 2 \times 10^4$ Ohm·cm. As a result, the resistance of the 0.5 cm diameter and 10 cm length water channel in the ceramic adapter is $\sim$1 MOhm.

The initial resistivity of LCW used for target cooling ρ^w may be specified as 200 kOhm·cm. As the water cooling system of a target is made from the high stable to corrosion steels and has not any copper, then it is reasonable to apply for target cooling the LCW used for horn cooling.

4.5 Helium or Vacuum inside the Target Casing?

Due to ionization of helium inside the casing, the target voltage will be equal to the horn voltage, which hinder Budal monitoring of a primary proton beam in the target. From this point of view it is more reasonable to have a vacuum inside the target casing.

As the horn voltage will be divided between two resistors R_{ct} and R_w, the resistance R_{ct} should be essentially larger than R_w, i.e. $R_{ct} \gg R_w$. For the 10 cm length water channel inside the ceramic adapter $R_w \simeq 1$ MOhm. The resistance of three target supports to the casing is defined by 30 μm alumina layer and is approximately equal to 5 MOhm. Maximum desirable value of R_{ct} may be calculated as $R_{ct} \leq 0.2T_0/C_{ct}$, where T_0 is the repetition period of beam spill. Calculation of C_{ct} gives $C_{ct} = 3.6$ nF, thus desirable value of $R_{ct} \simeq 100$ MOhm. Increasing of R_{ct} to this value may be achieved by an additional layer of the plasma sprayed alumina.

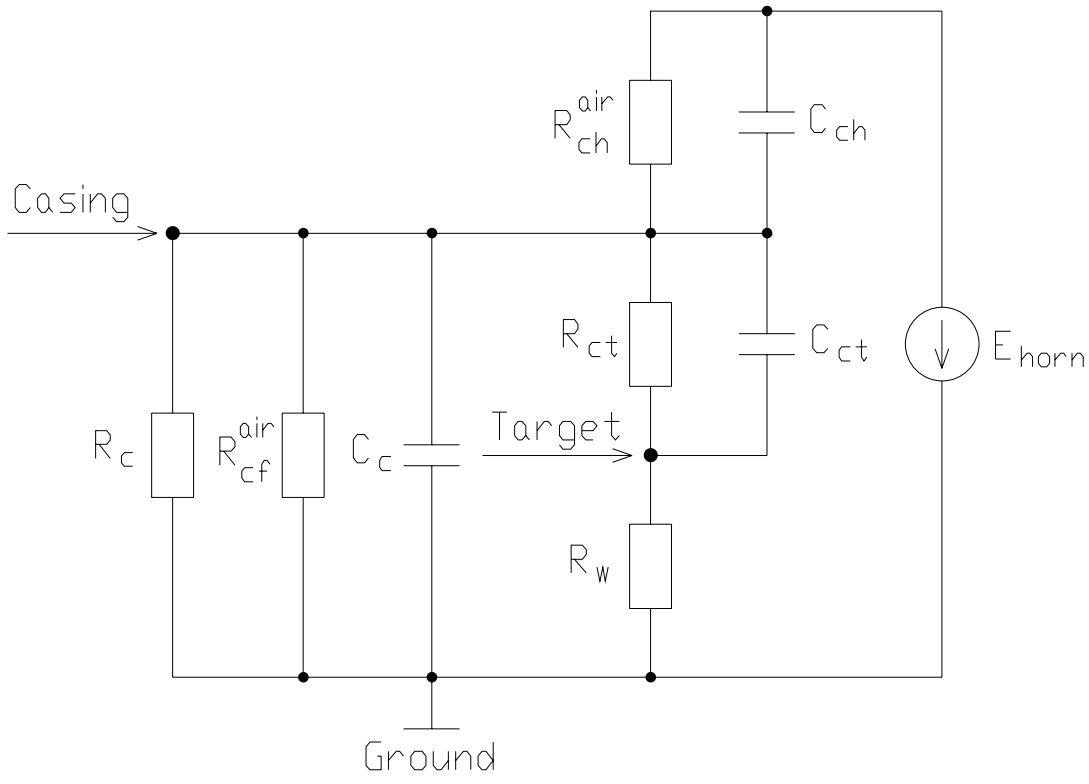

Figure 4.1: Equivalent electric circuit of the LE target.

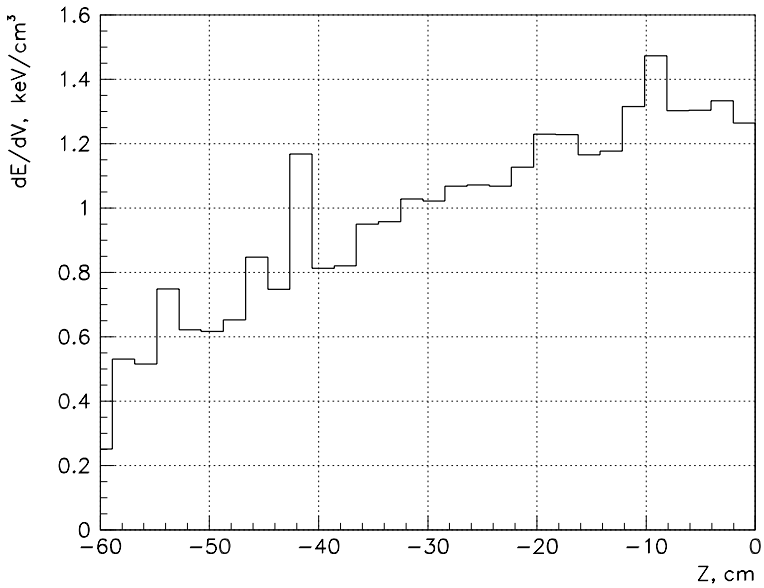

Figure 4.2: Distribution of the energy deposition density in the air along the target. $Z = 0$ corresponds to the downstream end of the target.

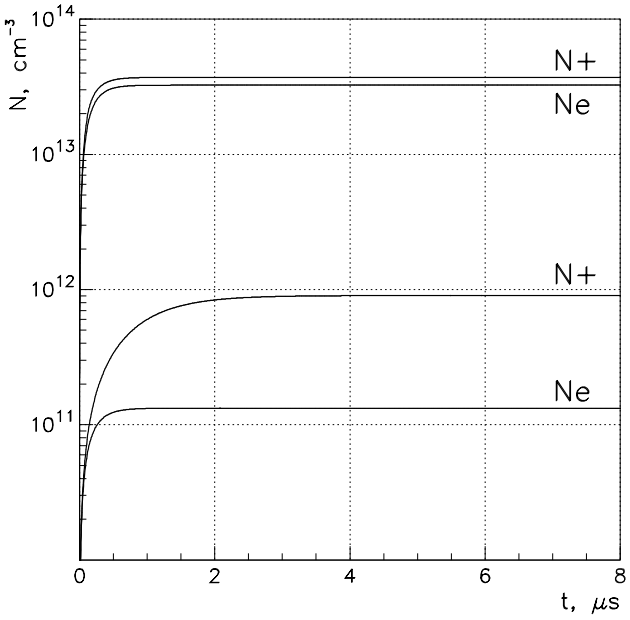

Figure 4.3: Instant densities of positive ions (N_+) and electrons (N_e) in air gaps between the horn and target casing (upper lines), and between target casing and the flange of target canister (lower lines) during the beam spill; $r_i = 10^{-6}$ cm^3/s, $r_e = 10^{-8}$ cm^3/s.

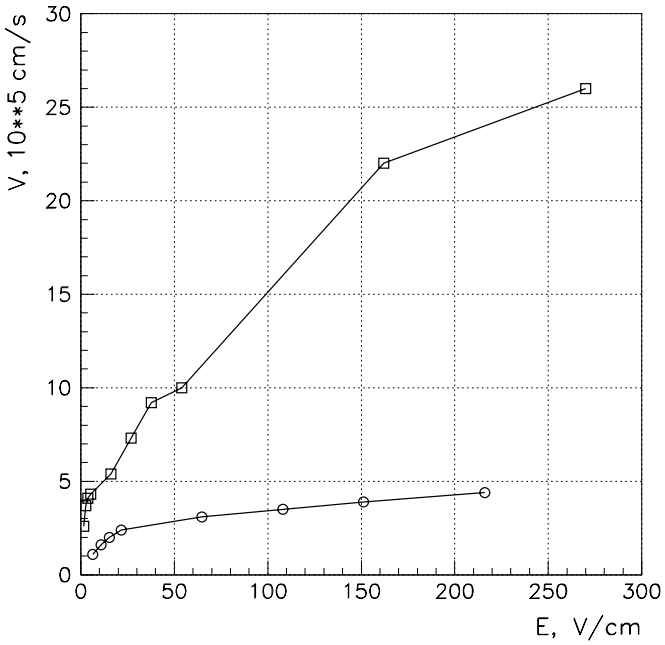

Figure 4.4: Drift velocities of electrons in oxygen (boxes) and nitrogen (circles) as functions of the electric field strength.

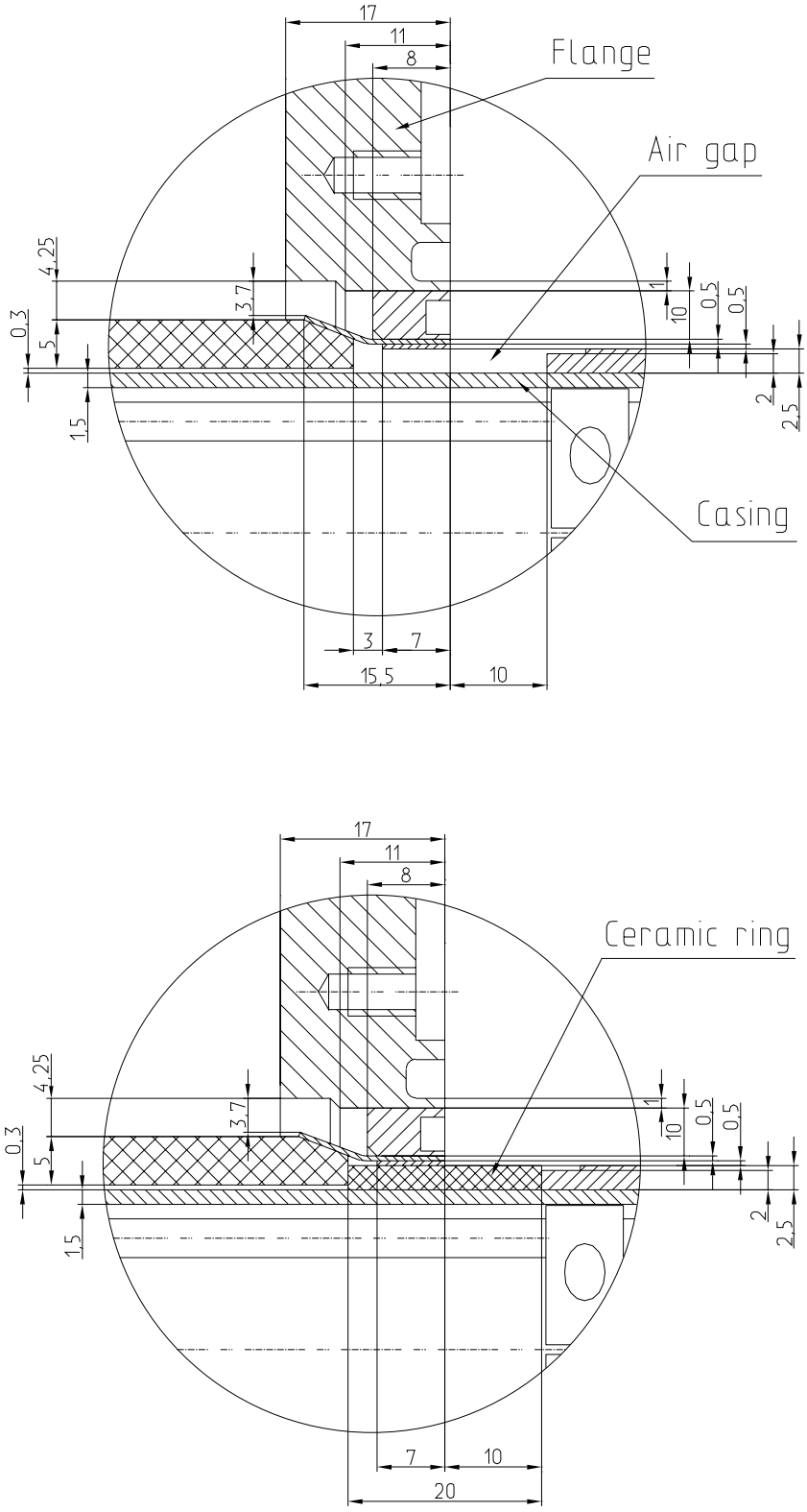

Figure 4.5: Some details of a target design near the ceramic adapter.

5 Some Specific Questions of a Target Design

5.1 Vacuum Pumping of a Target

Calculations of vacuum pumping of a target were made at the following conditions:

- the likely achievable vacuum inside the target casing should be between 10^{-2} and 10^{-3} Torr or 1.33 and 0.133 Pa. This vacuum is desirable to minimize an impact of residual gas ionization on the Budal signal;
- target casing with a target core was considered as a long system with distributed gas load. Out-gassing rates for different materials was taken at the room temperature (20°C): for graphite $q_c = 10^{-3}$ m^{3}Pa/m^2/s, for aluminum and stainless steel $q_{al,st} = 10^{-5}$ m^{3}Pa/m^2/s. Total out-gassing for such values of out-gassing rates is defined mainly by graphite: $Q = 5.5 \times 10^{-5}$ m^{3}Pa/s.
- pumping of a target is produced through two 3.5 m length stainless steel pipes with the internal diameter of 14 mm.

Results of calculations may be summarized as:

- the effective pumping speed is defined mainly by the conductance of pipes connecting the target canister with the pump located at the top of shielding. For nominal pumping speed about $S_p \sim 2 \times 10^{-2}$ m^3/s at the ultimate pump pressure $P_p = 1.33 \times 10^{-3}$ Pa (10^{-5} Torr) it is equal to $S_{eff} = 2.23 \times 10^{-4}$ m^3/s;
- the vacuum at the upstream end of target casing is defined by graphite out-gassing Q and by S_{eff}: $P_{up} = Q/S_{eff} = 2.47 \times 10^{-1}$ Pa ($\sim 5 \times 10^{-3}$ Torr). Pressure in the downstream end of target casing is greater than this value at 10^{-2} Pa;
- the estimated pump down time from atmosphere to the vacuum about 13.3 Pa (10^{-1} Torr) is about 5 minute, from 13.3 Pa to 2.47×10^{-1} Pa is approximately half an hour.

One should note that it is impossible to estimate the vacuum inside the target casing during beam hitting of graphite as there are no data on out-gassing of graphite at a high temperature. Target pumping at the stage of

intensive out-gassing due to beam hitting may be produced by the turbo-molecular pump. After decreasing of out-gassing it is more reasonable to use the sputter-ion pump.

The strength and stability of the target casing with a vacuum inside were tested experimentally by out-pumping of the 50 cm length part of aluminum pipe, which is planned to be used for vacuum casing. Two types of tests were performed:

- out-pumping during 4 min up to the vacuum of 10^{-2} Torr, the 2 min steady state and then filling the tested pipe with air. This was repeated 100 times;
- the tested pipe were held with vacuum during one week.

No changes in the shape of tested pipe were detected after both tests.

5.2 Stresses in the Ceramic Adaptor of Target Casing

Stresses in the ceramic adapter were calculated by the ANSYS taking into account the weights of all units of design: target casing, ceramic adapter itself, target core with cooling pipes, transition from an aluminum to a stainless steel, stainless steel ring welded to the adapter. Calculations show that maximal tensile stress is equal to 1.3 MPa, that is at least 100 times lower than the ultimate tensile strength of a high alumina ceramic.

6 Alignment of a Target during its Insertion into the Horn

6.1 Visual Control Using the TV-camera

The principle of a target alignment in the process of its insertion inside the horn is shown in Figure 6.1. Video camera and mark 1 are aligned in such a way that the axis passing through the video camera and mark 1 (the VC–M1 axis) is parallel to the target axis with both axes being in the vertical plane. Mark 2 and mark 3 (screen mark) are mounted on the horn and the M2–M3 axis is parallel to the horn axis in the vertical plane too. The distance between M2–M3 and horn axes should be equal to the distance between VC–M1 and target axes.

The accuracy of target alignment with respect to the horn is defined by:

- the accuracy δ_t of VC–M1 axis location with respect to the target axis;
- the accuracy δ_h of M2–M3 axis location with respect to the horn axis;
- the accuracy of optic axis location in the video camera when varying its focal length. This accuracy should be tested by special measurements.

Calculations show, that to obtain the 0.1 mm discrete TV-image it is reasonable to use an objective with the focus of 200 mm and resolution of $\sim$50 pairs of lines per mm in combination with the 768×576 CCD matrix and 8.6×8.3 μm pixel size TV-camera. In this case the total rms deviation of overlapping of target and horn axes is $M_{tot} = (\delta_t^2 + \delta_h^2 + 0.1^2)^{0.5}$. Supposing $\delta_t \simeq \delta_h \simeq 0.1$ mm one can get $M_{tot} = 0.17$ mm, i.e. the maximal deviation of two axes will not exceed 0.35 mm with the probability of 0.95.

One should note that marks (targets) located on the horn should have a high radiation resistance. The best material for them is a metal.

6.2 Touch of the Horn by Target Casing

The other possible way to align the target with respect to the horn is a method of touch of the internal surface of horn by target casing in order to attain a good electric contact between casing and horn (Figure 6.2). Detection of an electric contact was made by the appearance of scope signal

from the $\sim$1 kHz sin-wave generator. It was found that the average momentum which provide a good electrical contact is 0.15 Nm. It corresponds to the sag of target casing about 15 μm. Figure 6.3 illustrates how the angle between horn and casing axes can be measured using this method. The accuracy achieved in these measurements was 0.24 ± 0.054 mrad.

One should note, that for this method of alignment the target axis should be parallel to the axial direction of a carriage movement, i.e. it should be carefully aligned at a special stand. This method, of course, excludes any oxides on the internal surface of horn, despite the fact that its testing was made using the 20 years old parabolic lens without any cleaning of its internal surface.

In practice, both considered methods can be applied in combination.

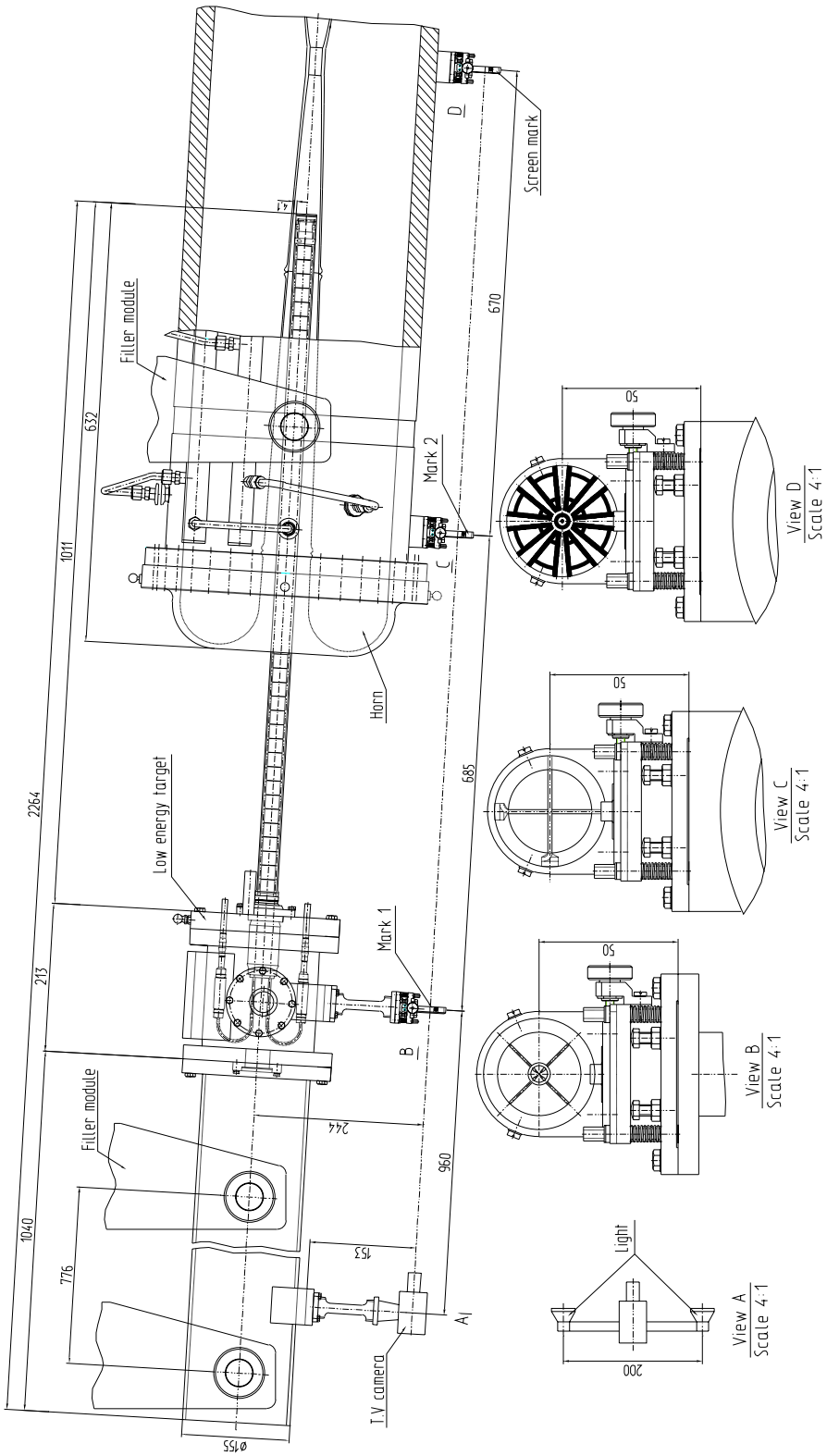

Figure 6.1: Insertion of target into the horn using the TV-camera.

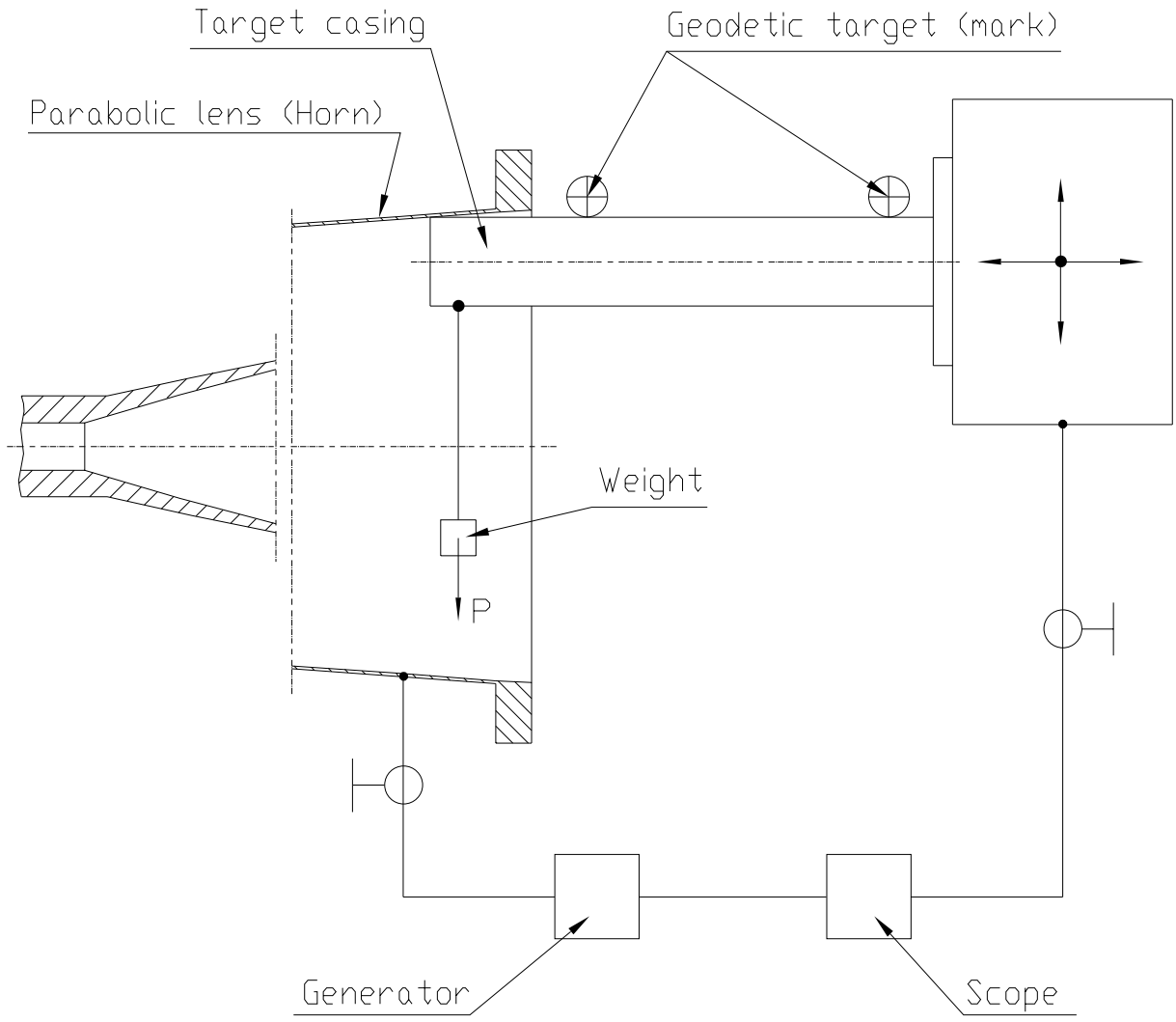

— Average momentum for a good contact - 0.15H·m
— Average deformation of the casing end at contact - 15 μm.

Figure 6.2: Detection of touch between the target casing and horn internal surface.

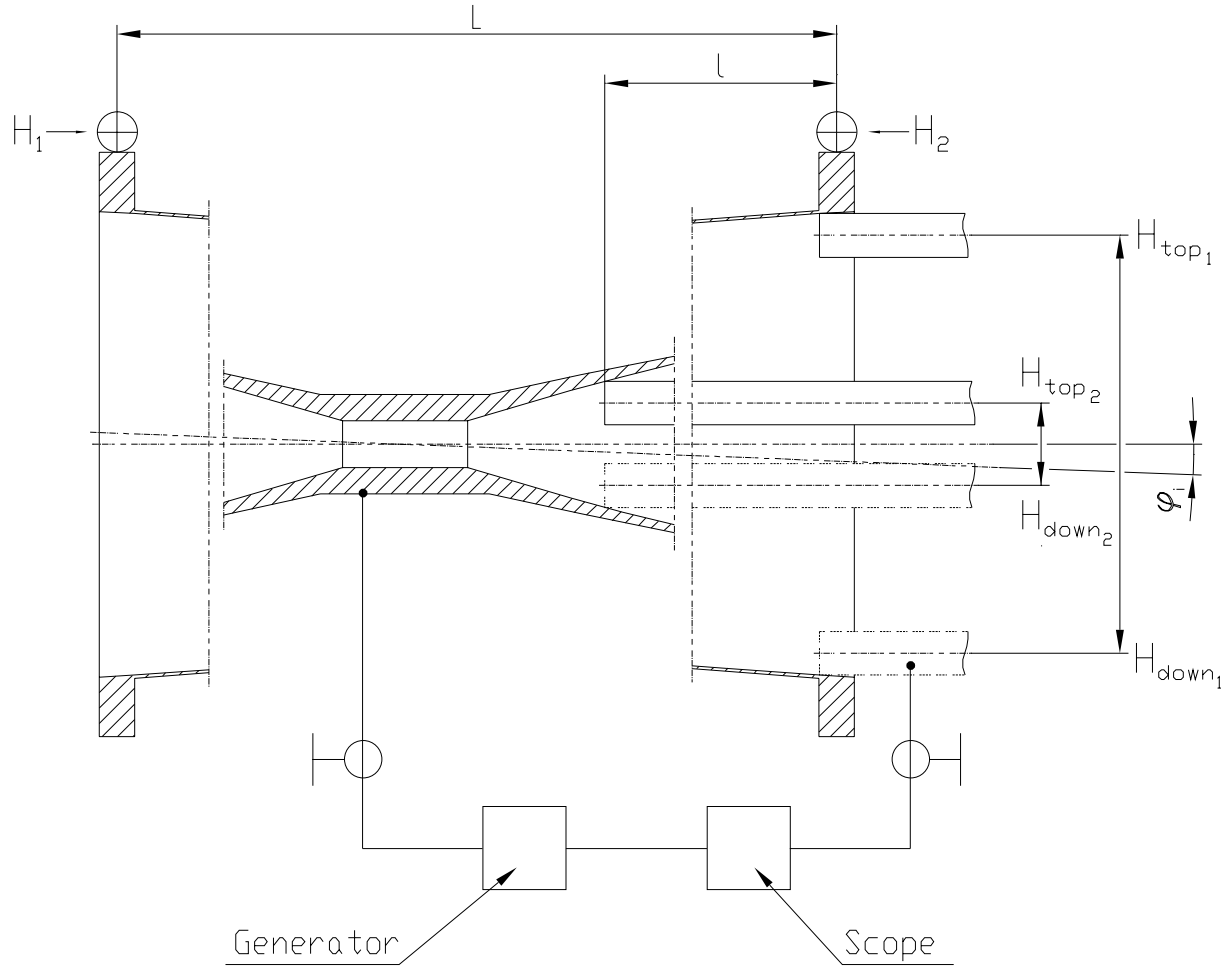

Sizes were measured:

$\Delta H = H_1 - H_2$ - by geodetic level type Ni 002 with accuracy ±0.07mm;

ΔH_{el} - by incrimental linear transducer "Heidenhain" with accuracy ±0.001mm;

L - by steel band with accuracy ±0.5mm;

l - by incrimental linear transducer "Heidenhain" with accuracy ±0.001mm.

$\varphi_{geod.} = 3.02 \pm 0.05 mrad.$

$\varphi_{el} = 2.78 \pm 0.02 mrad.$

$\varphi_{geod.} - \varphi_{el} = 0.24 \pm 0.054 mrad.$

Figure 6.3: Measurements of angle between horn and target casing axes.

References

[1] Irradiation Damage in Graphite due to Fast Neutrons in Fission and Fusion Systems, IAEA-TECDOC-1154, IAEA, Vienna, Austria, 2000.

[2] Design Properties of Graphite, APT Material Handbook, volume 1, chapter 10.

[3] M.W.Thompson. Defects and Radiation Damage in Metals, Cambridge, The University Press, 1969.

[4] V.S.Barashenkov, V.D.Toneev. Interactions of High Energy Particles and Atomic Nuclei with Nuclei, Moscow, Atomizdat, 1972.

[5] F.Sauli. Principles of Operation of Multiwire Proportional and Drift Chambers, CERN 77-09, Geneva, 1977.

[6] A.V.Yeletsky, L.A.Palkina, B.M.Smirnov. Phenomena of Transfer in a Weakly Ionized Plasma, p.156, Moscow, Atomizdat, 1975.

[7] V.Veksler, L.Groshev, B.Isaev. Ionized Methods of Radiation Investigations, Moscow, 1950.

[8] I.S.Grigoriev, E.Z.Meilikhov. Physical values, Moscow, Energoatomizdat, 1991.

[9] K.Bourkland, Private communication.